Thermal analysis of a compression heat pump-assisted solar still for Caspian regions of Kazakhstan

D. Baimbetov[1,2] · Ye. Karlina[1] · Ye. Yerdesh[1] · S. Syrlybekkyzy[3] · A. Toleukhanov[4] · M. Mohanraj[5] · Ye. Belyayev[1]

Abstract

Water scarcity is a major issue in cities situated at the Caspian regions of Kazakhstan. To overcome this issue, two compression heat pump-assisted solar thermal desalination configurations are proposed in this research. A numerical model using the TRNSYS simulation package was developed to predict the energy performance of the proposed systems and was validated with experimental results available in the open literature. The influence of ambient parameters and water depth in the basin of a solar still and insulation thickness was analyzed. The performance of proposed configurations is compared with conventional solar still. The errors noticed at 2 and 10 cm depths are 23.6% and 12.1%, respectively. The simulation results confirmed that the heat pump-assisted regenerative solar still configuration has a 91.1%, 73.0%, 61.6% and 82.6% improved productivity during winter, spring, summer and autumn climates, respectively. The results confirmed that significant improvement in freshwater production was observed with heat regeneration compared to the configuration without heat regeneration. The maximum freshwater production with heat regeneration reached 18.0 kg m^{-2} day^{-1} in summer and 9.0 kg m^{-2} day^{-1} in winter. The optimal water depth in the basin is observed to be in the range between 0.5 and 2.0 cm, while the insulation thickness is between 5.0 and 7.0 cm. The results confirmed that the proposed configuration satisfies the water requirements in Kazakhstan.

List of symbols

A	Area of glass/water/plate [m^2]
C	Specific heat capacity of glass/water/plate [J kg^{-1} °C^{-1}]
G	Acceleration due to gravity [m s^{-2}]
Gr	Grashof number
H	Heat transfer coefficient [W m^{-2} °C^{-1}]
$h_{\text{t,w-g}}$	Overall heat transfer coefficient from water surface to the inner surface of glass cover [W m^{-2} °C^{-1}]
$h_{\text{c,abs-w}}$	Convective heat transfer coefficient from absorber plate to water [W m^{-2} °C^{-1}]
$h_{\text{c,g-anb}}$	Convection heat transfer from glass to ambient air [W m^{-2} °C^{-1}]
$h_{\text{r,w-g}}$	Radiation heat transfer from water to glass [W m^{-2} °C^{-1}]
$h_{\text{e,w-g}}$	Evaporation heat transfer between water and glass [W m^{-2} °C^{-1}]
$h_{\text{c,w-g}}$	Convective heat transfer coefficient from water to glass [W m^{-2} °C^{-1}]
$h_{\text{r,g-amb}}$	Radiation heat transfer from glass to ambient air [W m^{-2} °C^{-1}]
$h_{\text{abs-amb}}$	Convection heat transfer from absorber plate to ambient air [W m^{-2} °C^{-1}]
h_{fg}	Latent heat of vaporization of water [J kg^{-1}]
$\dot{q}_{\text{ref}}$	Heat transfer by evaporator of refrigerant [W m^{-2}]
$\dot{q}_{\text{evaporator}}$	Heat transfer by evaporator [W m^{-2}]
H_{w}	Water depth in basin [m]
$I(t)$	Solar radiation [W m^{-2}]

✉ Ye. Belyayev
yerzhan.belyayev@gmail.com;
yerzhan.belyaev@kaznu.edu.kz

1 Department of Mechanics, Al-Farabi Kazakh National University, Almaty, Kazakhstan

2 Department of Energy and Automation, Sh. Yessenov Caspian University of Technology and Engineering, Aktau, Kazakhstan

3 Department of Ecology and Geology, Sh. Yessenov Caspian University of Technology and Engineering, Aktau, Kazakhstan

4 Department of Mechanical Engineering, Satbayev University, Almaty, Kazakhstan

5 Department of Mechanical Engineering, Hindusthan College of Engineering and Technology, Coimbatore, India

K	Thermal conductivity [W m^{-1} °C^{-1}]
$L_{abs/ins}$	Thickness of plate/insulation [m]
L_w	Length of water surface [m]
M	Mass [kg]
$\dot{m}_{ew}$	Instantaneous productivity [kg m^{-2} s^{-1}]
M_{ew}	Daily productivity [kg m^{-2}·day^{-1}]
P	Pressure [N m^{-2}]
Pr	Prandtl number
Ra	Rayleigh number
R_g	Reflectivity of glass cover
R_w	Reflectivity of seawater
S	Salinity [g kg^{-1}]
Switch	Evaporator on/off
T	Time [s]
T	Temperature [°C]
$U_{abs-amb}$	Overall heat transfer coefficient from absorber plate to ambient [W m^{-2} °C^{-1}]
V_{amb}	Velocity of wind [m s^{-1}]
W_w	Width of water cover [m]

Abbreviations

UN	United Nations
CA	Central Asia
RO	Reverse osmosis
MED	Multiple-effect distillation
MVC	Mechanical vapor compression
MSF	Multi-stage flash distillation
RES	Renewable energy system
CHP	Compression heat pump
TDS	Thermal desalination system
CSS	Conventional solar still
PCM	Phase change material
PW	Paraffin wax
HS	Hydrate salt
CGS	Crushed gravel sand
BSS	Biomass evaporator-assisted solar still
TRNSYS	Transient system simulation
TEV	Thermostatic expansion valve
DHW	Domestic hot water
ODE	Ordinary differential equation

Greek symbols

A	Absorptivity coefficient
α'	Fraction of solar flux coefficient
β	Thermal expansion coefficient
ε_g	Emissivity of glass cover
ε_w	Emissivity of seawater
ε_{eff}	Effective emissivity between water surface and glass cover
P	Density [kg m^{-3}]
M	Water dynamic viscosity [Ns m^{-2}]
Σ	Stefan–Boltzmann constant [W m^{-2} K^{-4}]
η_{th}	Efficiency

Subscripts

abs	Absorber plate
amb	Ambient
avg	Average
C	Convection
E	Evaporation
Ev	Evaporator
I	Glass/water
ins	Insulation
G	Glass
Th	Thermal
R	Radiation
Ref	Refrigerant
W	Water

Introduction

Kazakhstan is a non-coastal country with limited water resources. Aktau is a city with a human population of 281,805 located in the western part of Kazakhstan and has a huge water shortage. The water requirement is increasing rapidly in Aktau city due to an increase in human population. The water available in the Caspian Sea is the only source to meet the demand. The water available in the Caspian Sea is not possible to consume directly. The two commercial desalination plants presently available in Aktau City are: (i) reverse osmosis capable of producing 30,000 m^3 day^{-1} and (ii) thermal desalination capable of producing 46,000 m^3 day^{-1}. Reverse osmosis desalination has drawbacks such as water wastage, membrane cost, and membrane failures in winter due to frosting. Thermal desalination systems have more carbon emissions due to the burning of fossil fuels for evaporating water [1]. Therefore, it is necessary to identify an energy-efficient and environment-friendly solution for producing potable water. Earlier research investigations confirmed that solar energy is a viable option to integrate with thermal desalination systems to enhance the evaporation processes. Similarly, many research studies have confirmed that compression heat pumps (CHP) are energy-efficient devices used for regenerating waste heat for heating saline water [2]. The review of selected studies reported on energy-efficient and environment-friendly desalination techniques is presented in this section.

In a solar still thermal desalination system (SSTDS), the water is purified by evaporating the saline water using solar energy and condensed over the bottom surface of a glass to get distilled water [3, 4]. However, SSTDS has the maximum distilled water production of 3 ± 1 L day^{-1} m^{-2}, which is inadequate for domestic requirements. The distilled water production using SSTDS was improved to about 6 L day^{-1} m^{-2} using sensible heat storage materials like sand [5], pebbles [6], gravel [7], and iron scraps [8]. Further, the latent

heat storage materials (like paraffin wax) were used to store heat excess heat harvested during sunshine hours and utilized during low and off sunshine hours and improved the freshwater production up to 7 L day^{-1} m^{-2} [9, 10]. Sakthivel et al. [11] increased the fresh distilled water production of SSTDS to 4 L day^{-1} m^{-2} using a jute regenerative medium. The jute medium used in the basin of SSTDS has regenerated the waste heat released during the condensation of water vapor. The fresh distillate water production and energy efficiency were improved by 20% and 8%, respectively. The plate fins and pin fins were used in the basin of SSTDS to increase freshwater production by increasing the heat-absorbing area and harvesting more solar thermal energy [12, 13]. The fresh distilled water production in SSTDS was improved significantly using nano-coating over the basin of SSTDS and by adding the nanoparticles to saline water [14]. The influence of the magnetic field created by a ceramic magnet has increased the evaporation rate and resulted in 19.6% improved fresh distilled water production compared to the conventional SSTDS [15]. The maximum fresh distillate water production in SSTDS using heat storage materials in the basin, nano-coating, and heat regenerative medium was improved to 7 L day^{-1} m^{-2}, which is not enough for daily domestic requirements.

The addition of auxiliary equipment like solar air collectors, solar water collectors, heat pipes, biomass heaters, and heat pumps has improved fresh distilled water production significantly. The integration of solar air collectors with SSTDS has improved freshwater production to 4 ± 1 L day^{-1} m^{-2} by preheating the air before entering the solar still [16–18]. Similarly, the solar water collectors were used to preheat the saline water before entering the basin of a solar still and improve freshwater production by 4 ± 1 L day^{-1} m^{-2} [19–21]. The integration of solar-assisted air and water collectors with SSTDS has improved freshwater production and tackled the limitations associated with air and water-based collectors [22–24]. The use of heat pipes in solar stills has improved freshwater production to 7 day^{-1} m^{-2} [25, 26]. The use of biomass heaters with SSTDS has improved distilled water production to 6 L day^{-1} m^{-2} [27, 28]. However, heat regeneration is not possible in the case of heating equipment reported in this section.

The CHP systems are energy-efficient heating equipment capable of delivering more heat than input work it consumes for its operation and possibly regenerating the waste heat released during condensation of water vapor [29]. The CHP-SSTDS has significantly improved fresh distilled water production compared to the conventional SSTDS by regenerating the heat accumulated inside the solar still. Many research studies have been reported on CHP-SSTDS. In related research, Hawlader et al. [30] studied the performance of a CHP-assisted TDS and reported a maximum coefficient of performance (COP) of 8.0 and a maximum hourly fresh distillation water production of 1.38 kg. Hidouri et al. [31] proposed a CHP-SSTDS to increase the fresh distillate output to 12 L m^{-2}, which is 80% higher than conventional SSTDS. Similarly, Halima et al. [32] made a parametric simulation of a CHP-SSTDS. It was reported that the system has a maximum fresh distillate water production of 12 L m^{-2} at a water depth of 10 mm. The polyurethane of 10 mm thick was selected as a suitable insulation material for the basin. Belyayev et al. [33, 34] reported that hydrate salt is a suitable phase change material for the basin of a CHP-SSTDS used in low ambient conditions due to its low melting temperature. Hidouri and Mohanraj [35] reported that CHP-SSTDS has 85% improved freshwater production than conventional SSTDS with an internal exergy of about 7.5%. The performance of a CHP-SSTDS was experimentally investigated under Indian climatic conditions [1]. The basin of SSTDS was covered by paraffin wax phase change material. Their results reported the maximum daily fresh distillate water production of 16.0 kg with additional hot water production of 100 L at about 48 ℃. The cost of freshwater distillate was estimated at 0.05471 USD/Liter. Sivakumar et al. [36] integrated the CHP with solar air collector and SSTDS and tested its performance under Indian climatic conditions. Their proposed system has produced the maximum and minimum freshwater distillates of 22 and 19.5 L day^{-1} during summer and winter, respectively. The freshwater production cost per liter was reported as 0.046 USD. Sharshir et al. [37, 38] developed and tested the performance of a CHP-SSTDS for producing fresh distillate water and refrigeration effect simultaneously. It was reported with a maximum freshwater distillate of 10.14 L m^{-2} and freshwater production cost of 0.0136 USD/Liter. The cold room space temperature reached 12.8 ℃ lower than ambient. All these studies involve complete or partial heat regeneration through either complete preheating of saline/brackish water [31–34] or partial heating with additional heating [1] or refrigeration [37, 38]. However, there are no comparative analyses in the literature to study the effect of regeneration with different configurations of the connection between CHP and a conventional SS on freshwater productivity.

The cited literature review confirmed that CHP-SSTDS has increased distilled water production with improved energy performance compared to conventional SSTDS. Nevertheless, comparative studies on the effects of different CHP connections to SSTDS on freshwater productivity are not reported in the open literature. Moreover, studies of the heat regeneration effect in CHP-SSTDS in four-season climates have been poorly investigated. The present research numerically explores this comparison for the CHP-SSTDS system at Aktau City in the Caspian region of Kazakhstan. For these purposes, the previously created numerical calculation algorithm was modified and a component for the

CHP-SSTDS was created in the TRNSYS 18.0 software [39]. This paper presents a comprehensive mathematical model of the system based on the first law of thermodynamics using standard coefficients. The calculation algorithm was verified by comparing it with experimental data from other authors found in the open literature [40]. The presented mathematical model and calculation algorithm will serve for further feasibility study, development, and testing of our experimental setup and can also be replicated by other researchers.

System description

The schematic diagram of the CHP-SSTDS is depicted in Fig. 1a–b, illustrating two different configurations with and without heat regeneration. The heat pump component of the CHP-SSTDS system comprises a hermetically sealed reciprocating compressor (using R134a refrigerant), a copper coil condenser on the refrigerant side, a thermostatic expansion device (TEV), and a roll-bond-type evaporator located inside the SS. Additionally, the heat pump is equipped with a sealed-type refrigerant drier, a liquid receiver, a sight glass, pressure gauges, and a pressure switch. In the first configuration, a roll-bond evaporator extracts heat from inside the SS cabin and transfers it to heat the water in the tank (see Fig. 1a). In this case, there is no preheating of basin water
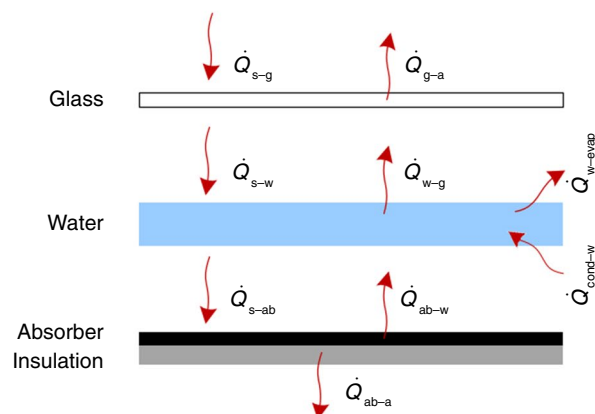
Fig. 1 Schematic diagrams of proposed heat pump-assisted solar stills
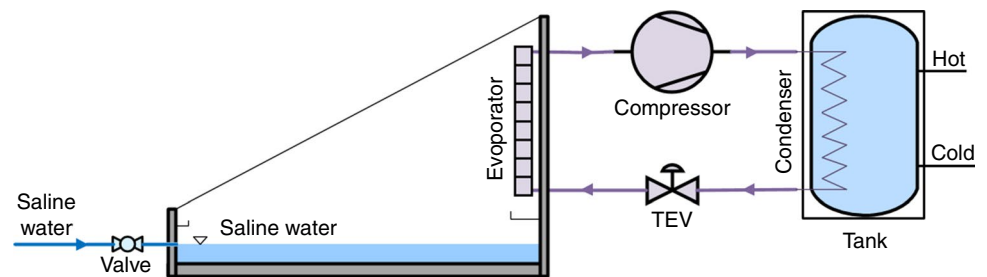
(a) Schematic view of the heat pump water heater-assisted solar still (Type 1)
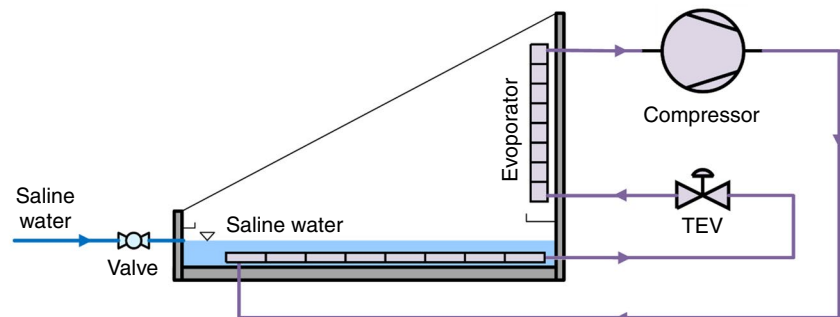
(b) Schematic view of the heat pump-assisted regenerative solar still (Type 2)

(c) Heat transfer mechanisms inside the solar still

in the SS cabin. In contrast, in the second configuration, a roll-bond evaporator extracts heat from the SS cabin and, after conversion, regenerates it through the condenser into the basin water (see Fig. 1b). In this case, the heat extracted from the cabin is regenerated by heating the basin water.

The conventional SS is a single slope solar still with a tilt angle of 33º facing south. The basin area is 1 m², accommodating saline water with depths of up to 20 cm. Water vapor condenses on the inner surface of the SSTDS glass and on the surface of the CHP roll-bond evaporator. From these two surfaces, distilled water flows into separate trays and is collected in two jars. Saline water enters the SSTDS by adjusting the manual valve. The tank (see Fig. 1a) serves as a condenser for CHP and a water heater for domestic hot water (DHW) applications. Figure 1c illustrates the main heat transfer mechanisms in SSTDS.

Mathematical model

The mathematical model is an ODE system constructed based on the heat balance of the CHP-SSTDS components. The fundamental heat balance equation was formulated for the glass cover of the SS, saline/brackish water, absorber plate, and roll-bond evaporator. The following assumptions were considered in energy performance modeling:

i. Water vapor leakages are ignored.
ii. Influence due to potential, kinetic, and chemical energies is ignored.
iii. The saline water temperature in the basin was assumed to be uniform.
iv. The capacities of the heat pump's evaporator and condenser were assumed to be uniform, and the entire surface of the evaporator was also assumed to be uniform.
v. The thermal-physical properties of glass, water, absorber plate, roll-bond evaporator, and insulation materials presented in Table 1 were considered for calculations [41].

The first law of thermodynamics is employed to formulate the heat balance equations for the CHP-SSTDS components. As per the heat balance, the quantity of inlet heat to a specific component of the system equals the sum of outlet heat and stored heat within this component. Figure 1c depicts a schematic representation of the heat balance within the conventional SS. For a glass cover, the incoming heat comprises solar irradiation and heat from the water surface, while the outgoing heat includes convective heat transfer with the ambient air and radiative heat transfer with the sky. The general energy balance equation for a glass cover is given by:

Table 1 Characteristics of the heat pump-assisted regenerative solar still

Relevant parameters	Numerical value	Unit
α_g [32]	0.0475	
α_w	0.3	
α_{abs}	0.95	
R_g [33, 34]	0.0735	
R_w	0.025	
ε_g [32]	0.95	
ε_w	0.94	
A_g	1.1547005384	m²
A_w	1	m²
A_{abs}	1	m²
A_{ev}	0.5	m²
L_{abs}	0.002	m
L_{ins}	0.05	m
H_w	0.05	m
L_w	1	m
W_w	1	m
K_{abs}	16.3	W m^{-1}°C^{-1}
K_{ins}	0.039	W m^{-1}°C^{-1}
$\dot{q}_{evaporator}$ *(R134a)*	800	W m^{-2}
Switch	(0;1)	
C_g	800	J kg^{-1}°C^{-1}
C_{abs}	480	J kg^{-1}°C^{-1}
C_{ev}	385	J kg^{-1}°C^{-1}
m_g	11.685569448398	kg
m_{abs}	15.6	kg
M_{ev}	3.675	kg
σ	5.6697×10^{-8}	W m^{-2} K^{-4}
g	9.81	m s^{-2}
S	13	g kg^{-1}
t	30	s

$$\alpha'_g I(t) A_g + h_{t,w-g} A_w (T_w - T_g) - h_{c,g-amb} A_g (T_g - T_{amb})$$

$$-h_{r,g-amb} A_g (T_g - T_{amb}) = (m_g C_g)\left(\frac{dT_g}{dt}\right), \quad (1)$$

where $\alpha'_g = (1 - R_g)\alpha_g$ is a fraction of the solar flux coefficient, representing the absorbency of glass. The overall heat transfer coefficient due to radiation, convection [41], and evaporation [42] is given by the following equation [33, 34]:

$$h_{t,w-g} = h_{r,w-g} + h_{c,w-g} + h_{e,w-g} \quad (2)$$

Here, the heat transfer coefficients are determined by the following equations:

$$h_{r,w-g} = \varepsilon_{\text{eff}}\sigma \left[\frac{(T_w + 273.15)^4 - (T_g + 273.15)^4}{T_w - T_g} \right] \quad (3)$$

$$h_{c,w-g} = 0.884 \left[T_w - T_g + \frac{(P_w - P_g)(T_w + 273.15)}{268.9 \times 10^3 - P_w} \right] \quad (4)$$

$$h_{e,w-g} = 0.016273 \cdot h_{c,w-g} \left[\frac{P_w - P_g}{T_w - T_g} \right] \quad (5)$$

The convective heat transfer coefficient between the glass and ambient air is determined using Eq. (6):

$$h_{c,g-amb} = 2.3 + 3V_{amb} \quad (6)$$

The radiative heat transfer coefficient between the glass and ambient air is determined using Eq. (7):

$$h_{r,g-amb} = \varepsilon_g \sigma \left[\frac{(T_g + 273.15)^4 - (T_{amb} + 273.15)^4}{T_g - T_{amb}} \right] \quad (7)$$

For saline/brackish water, the inlet heat comprises solar irradiation and convective heat transfer between the absorber plate, while the outlet includes heat exchange between the water and glass, and heat exchange between the water and the roll-bond evaporator. Equation (8) represents this heat balance for saline water:

$$\alpha_w' I(t)A_w + h_{c,\,abs-w}A_{abs}(T_{abs} - T_w) - h_{t,w-g}A_w(T_w - T_g)$$
$$- A_{ev}\dot{q}_{ref} = (m_w C_w)\left(\frac{dT_w}{dt}\right), \quad (8)$$

where $\alpha_w' = (1 - R_g)(1 - \alpha_g)(1 - R_w)\alpha_w$ is a fraction of solar flux coefficient, representing the absorbency of saline water. $m_w = A_w \cdot H_w \cdot \rho_w$ is the water mass, where water density is assumed to be at 25 ℃. The convective heat transfer coefficient between water and the absorber plate is determined using Eq. (9) [43]:

$$\begin{cases} h_{c,abs-w} = 0.54 \cdot \left(\frac{k_w Ra_w^{\frac{1}{4}}}{L_w} \right), if\ Ra_w = 10^4 - 10^7, Pr \geq 0.7 \\ h_{c,abs-w} = 0.15 \cdot \left(\frac{k_w Ra_w^{\frac{1}{3}}}{L_w} \right), if\ Ra_w = 10^7 - 10^{11}, allPr \end{cases} \quad (9)$$

For the absorber plate, the inlet heat comprises solar irradiation, while the outlet includes convective heat transfer between the absorber plate and water, as well as heat loss from the rear side of the absorber, accounting for insulation. Equation (10) represents this heat balance for the absorber plate:

$$\alpha_{abs}' I(t)A_{abs} - h_{c,abs-w}A_{abs}(T_{abs} - T_w)$$
$$- U_{abs-amb}A_{abs}(T_{abs} - T_{amb})$$
$$= (m_{abs}C_{abs})\left(\frac{dT_{abs}}{dt}\right) \quad (10)$$

where $\alpha_{pl}' = (1 - R_g)(1 - \alpha_g)(1 - R_w)(1 - \alpha_w)\alpha_{abs}$ is a fraction of the solar flux coefficient, representing the absorbency of the absorber plate. The overall heat loss coefficient is determined using Eq. (11):

$$U_{abs-w} = \left[\frac{L_{abs}}{k_{abs}} + \frac{L_{ins}}{k_{ins}} + \frac{1}{h_{abs-amb}} \right]^{-1} \quad (11)$$

The convective heat transfer coefficient between the absorber plate and ambient air is determined using Eq. (12):

$$h_{abs-amb} = 5.7 + 3.8V_{amb} \quad (12)$$

The heat flux to the surface of the roll-bond evaporator of the heat pump is determined by Eq. (13):

$$\dot{q}_{ref} = \dot{q}_{evaporator} \cdot \text{Switch} \quad (13)$$

where Switch is the state of the evaporator: on or off, $\dot{q}_{evaporator}$ is the heat flux absorbed by the CHP evaporator (see Table 1). For Type 2, $\dot{q}_{condenser}$ is determined based on $\dot{q}_{evaporator}$ and the assumption that the COP is equal to 3.0.

The instantaneous productivity of the solar still is determined by [33, 34]:

$$\dot{m}_{ew} = \frac{\{h_{e,\,w-g}A_g(T_w - T_g) + A_{ev}\dot{q}_{ref}\} \cdot \Delta t}{A_w h_{fg}} \quad (14)$$

The daily productivity of the solar still is determined by [33, 34]:

$$M_{ew} = \sum_{day} \dot{m}_{ew} \quad (15)$$

The energy efficiency of the CHP-SSTDS is determined by Eq. (16) [33, 34]:

$$\eta_{th} = \frac{\sum \dot{m}_{ew}h_{fg}}{\Delta t \cdot A_{abs} \sum I(t)} \quad (16)$$

where h_{fg} is the latent heat of water vaporization, the calculation of which is detailed in Appendix A. In Eqs. (1)–(16), coefficients not listed in Table 1 have calculation formulas provided in Appendix A.

Solution method

The system of ODEs is solved using the fourth-order Runge–Kutta method [33, 34]. A computer program for the implementation of the numerical algorithm was developed using the Python 3.9.0 programming language. Additionally, the calculation algorithm was implemented on licensed software TRNSYS 18.0 [39]. Figure 2 depicts the TRNSYS simulation project, illustrating the system components. The performance simulation begins by 6:00 am and concludes at midnight in 30-s intervals, with specified weather data. The simulation begins with a "Weather'' (Type 9e) component that reads ambient air temperature, wind speed, and solar irradiation data from an external.txt file. The "T/Sr" (equation) serves as a validation component for checking the intermediate values of temperature and solar irradiation. Subsequently, these solar irradiation values are transferred to the "SR" (equation) component, where components of Eqs. (1), (8), and (10) such as:$\alpha'_g I(t)$,$\alpha'_w I(t)$,$\alpha'_{pl} I(t)$ are calculated. Subsequently, all preceding components are connected to the main component, where all Eqs. (1)–(16) are implemented in the "Solar still (with evaporator)" (custom-developed component). As a result, temperature, productivity, efficiency, heat flow, and heat transfer coefficients for the current iteration can be derived from this component. The "Temperature Last Time Steps" (Type93) component is designed to store the previous values of glass and water temperatures for transferring this data to the "Switch" (custom-developed component). The "Switch" component is responsible for activating or deactivating the heat pump, generating a logical signal of 0 or 1 at the output. This component is further elaborated below. These values are then transferred to the "Solar still" component for the subsequent iteration. Following this, the data from this component are displayed graphically (Type65d) and in text format (Type25c). These procedures are repeated at each time step.
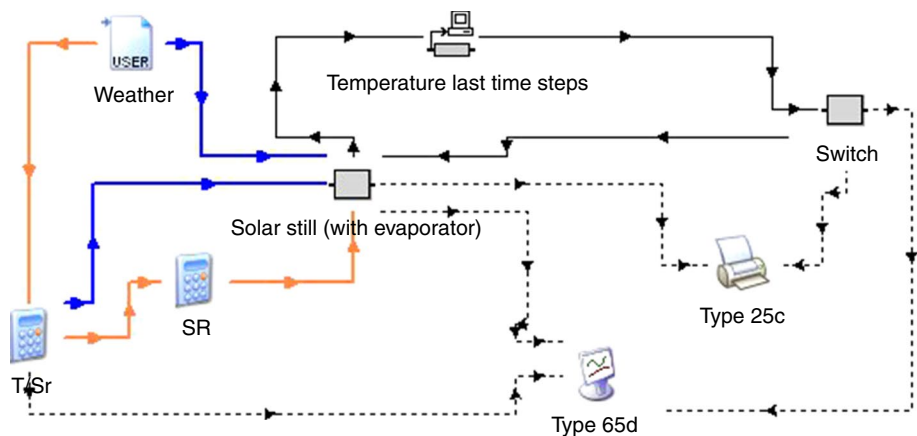
Figure 3 is a block diagram detailing the operation of the "Switch" component (refer to Fig. 2). Upon initial startup, the initial values of timers and switcher are configured. The variables timer and timer2 are responsible for preventing abrupt compressor on/off transitions and overheating of the heat pump, respectively. The timer variable is set to 5 min, representing the minimum time for being in the on or off state. The timer2 variable is set to 50 min, indicating the maximum time for being in the on state. The initial position of the "Switch" is set to zero. Subsequently, the previous values (initial values at the simulation start) of the water and glass temperatures are initialized. By setting the current simulation time, it is then compared with the end simulation time. If the time is less than or equal to the first timer (5 min), there is no change in this iteration. However, if the "Switch" is turned off and the temperature difference between the water and glass exceeds 2 ℃, then the "Switch" is turned on and the timers are updated. If the "Switch" is turned on and the time is greater than or equal to timer2, then the "Switch" turns off and the first timer is updated. Alternatively, if the "Switch" is turned on and the time is less than or equal to timer2, and the temperature difference between the water and glass is less than 0.5 ℃, then the "Switch" remains on and the first timer is updated. If the temperature difference conditions are not met, then no changes occur, and the 'Switch' and timers remain in their previous positions. In each iteration, data for the timer and switcher are saved for the next iteration. All geometric and thermophysical parameters of the CHP-SSTDS for calculations according to Eqs. (1)–(16) are presented in Table 1, with appropriate units indicated.

Model validation

To validate the numerical model, the obtained results were compared with experimental data reported by Agrawal et al. [40]. For the validation calculations, all geometric, physical,

Fig. 2 Transient system simulation project

Fig. 3 Flowchart of numerical calculation
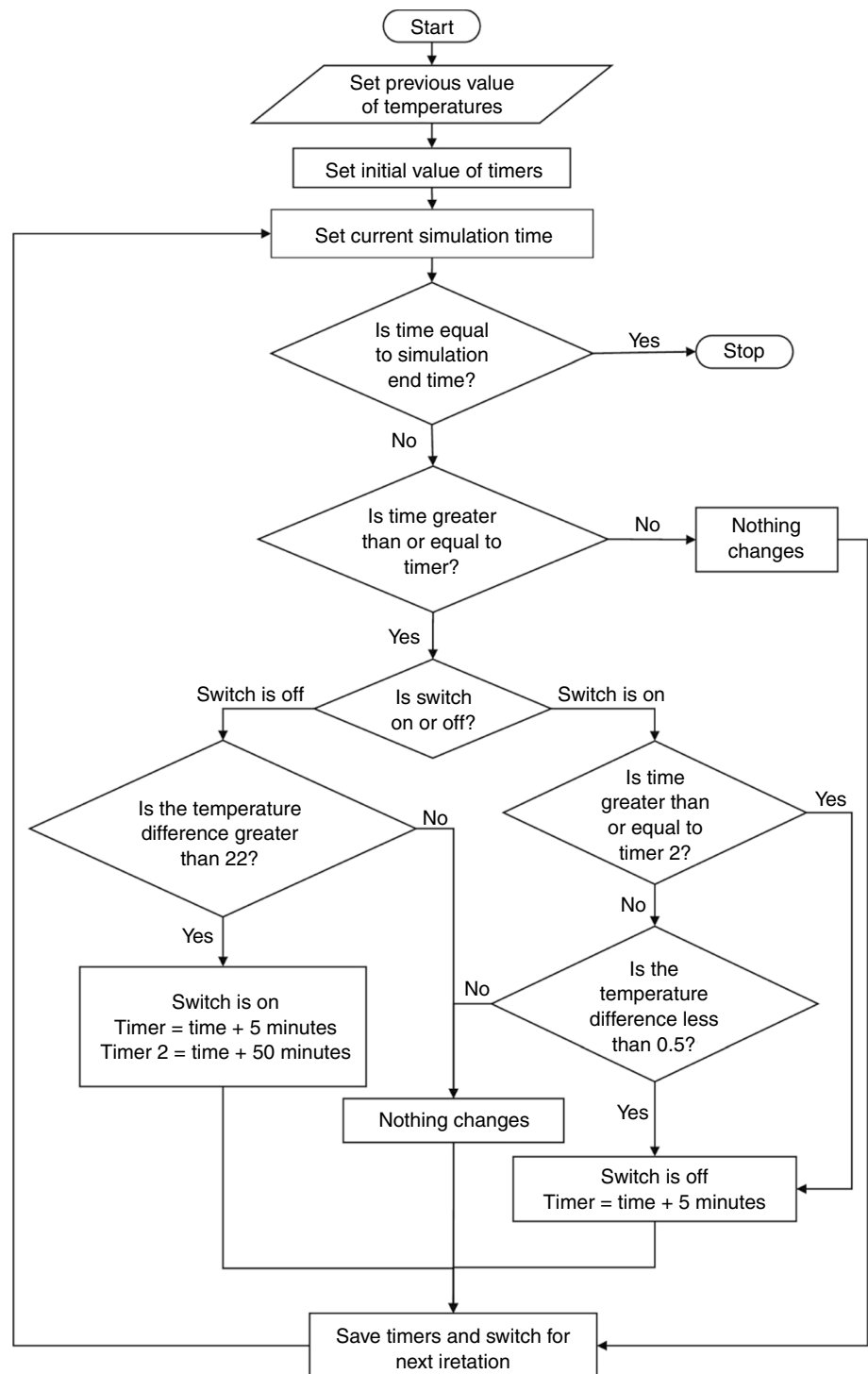
and thermal parameters were chosen by those specified in [40] for the SSTDS configuration, excluding the roll-bond evaporator. The weather data were adjusted to correspond with the experimental conditions reported in [40], reflecting the climate of Reva, India. Figure 4 illustrates the TRNSYS simulation project conducted for the validation scenario. In this particular case, components such as "Switch," "T/Sr,"

and "Temperature Last Time Steps" are not present. The system operation follows the established algorithm with minor variations. Additional components have been incorporated, including "Glass/Water (Experimental)" (Type9e), representing experimental data sourced from [40], and the "Error water/glass" (self-developed) component, designed to compute the disparity between numerical results and

Fig. 4 Transient system simulation project for validation
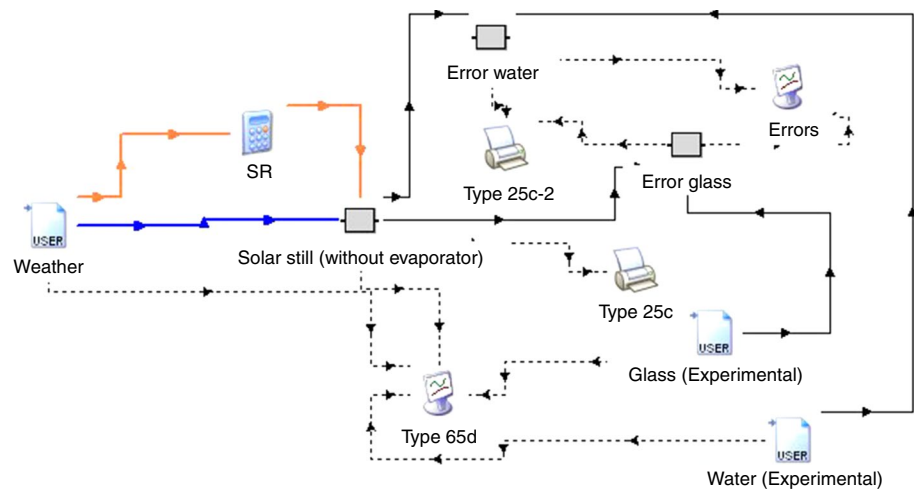
experimental observations. To visually depict the dynamic evolution of the error over time, the "Errors" component (Type65d) is employed. Furthermore, for a graphical comparison between the obtained temperatures and their experimental counterparts, all temperatures are plotted on a comprehensive graph (Type65d). Furthermore, the validation of numerical results obtained using TRNSYS was conducted by comparing them with the outcomes of the Python code. Consistently, identical numerical results were obtained in both cases.

In Fig. 5, the numerical and experimental values sourced from for the water and glass temperature were compared. The comparison was conducted based on the measured values at water depths of 2 cm, 4 cm, 6 cm, and 10 cm. Based on Fig. 5, the comparison between measured and calculated values demonstrates a close agreement. The minimum relative discrepancies between numerical and experimental values of water temperature are 6.26% at a depth of 2 cm, 6.32% at 4 cm, 0.0096% at 6 cm, and 0.0029% at 10 cm. Meanwhile, the maximum discrepancies are 23.62% at 2 cm depth, 22.72% at 4 cm, 18.96% at 6 cm, and 12.08% at 10 cm, respectively. It is evident that the maximum basin water temperature decreases noticeably with an increase in the depth of the basin water. The slower response to changes in temperature at greater depths of the basin is attributed to the elevated thermal inertia of the water mass [40]. As the depth of the basin water increases, there is a discernible shift in the peak basin water temperature toward afternoon hours, with this elevated temperature persisting into the evening. Consequently, a minor reduction in diurnal output and an augmentation in nocturnal output ensue.

As illustrated in Fig. 5, the variation trend of glass temperature closely mirrors that of the water temperature within the basin, owing to the incorporation of their heat exchange mechanism in the analysis. Nonetheless, disparities are evident in the maximum values of water temperature, particularly notable at shallower depths, where the variance

between measured and calculated values is comparatively less pronounced. Likewise, concerning glass temperature, the minimum relative discrepancies at depths of 2 cm, 4 cm, 6 cm, and 10 cm are 0.00077%, 0.0071%, 1.83%, and 0.002%, respectively. Correspondingly, the maximum relative discrepancies are 28.08%, 30.77%, 21.39%, and 14.26%, respectively. The mean relative error for water at depths of 2 cm and 4 cm is 16.11% and 13.54%, respectively, while for glass, it is 14.89% and 12.84%, respectively. Similarly, at depths of 6 cm, the mean relative errors are 7.95% for water and 9.27% for glass. At a depth of 10 cm, the mean relative errors are 5.68% for water and 4.65% for glass. For all the average values reported, it was observed that the medians are lower than the averages, indicating significant minimum discrepancies. It can be inferred that the validation process yielded favorable results.

Results and discussion

The numerical temperature variations across various components of a solar still and CHP-SSTDS (with and without heat regeneration) were predicted for the climatic conditions of Aktau City, situated on the eastern coast of the Caspian Sea in west Kazakhstan. In Fig. 6, the ambient data variations of Aktau City during four seasons of Kazakhstan (January, April, July, and October) are compared. The meteorological data were extracted from authoritative sources [44].

In Fig. 6a, the hourly variation of ambient temperature during January, April, July, and October months is compared. In January, the average ambient temperature varied from − 1.7 to 3.0 ℃, while in April, July, and October, the respective variations from 9.7 to 16.1 ℃, from 22.9 to 29.1 ℃, and from 12.5 to 17.3 ℃, respectively. The solar irradiation variations are depicted in Fig. 6b. The maximum average solar irradiation was 360 W m^{-2}, 625 W m^{-2}, 795.23 W m^{-2}, and 455.89 W m^{-2} for January, April, July,

Fig. 5 Comparisons of temporal temperature variations
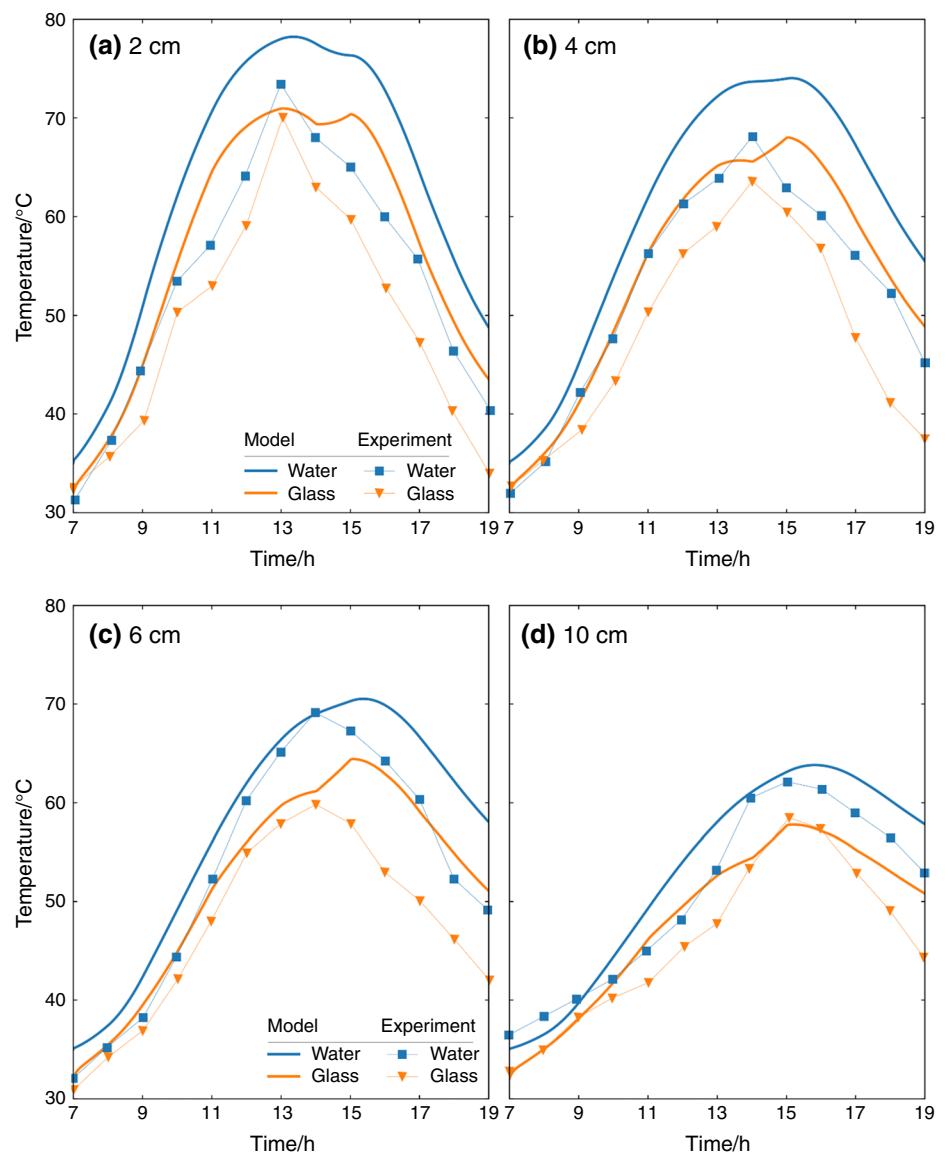
and October, respectively. Additionally, Fig. 6c illustrates the average wind speed distribution. In January, the average wind speed fluctuates between 6.32 m s^{-1} and 7.37 m s^{-1}, while in April, July, and October, the corresponding ranges are 4.31 m s^{-1} to 6.09 m s^{-1}, 4.33 m s^{-1} to 5.25 m s^{-1}, and 4.57 m s^{-1} to 6.51 m s^{-1}, respectively. Aktau City experiences clear and sunny conditions for more than 225 days annually, presenting an opportunity to utilize solar thermal energy technology for producing freshwater.

Figure 7 illustrates the temporal temperature variations across different components of the CHP-SSTDS under configurations Type 1, Type 2, and a conventional SSTDS system devoid of a heat pump. Figure 7a displays the temperature variation of distinct components within the CHP-SSTDS as a function of time over a January day. Based on the acquired numerical data, the temperature variations of the T_{abs}, T_{g}, and T_{w} exhibit analogous trends in both the

conventional SS and Type 2 configuration. These trends entail a gradual increase throughout the day, culminating in peak values typically observed between 3:00 pm and 4:00 pm, followed by a gradual decline. In comparison, the temperature distribution observed in Type 1 markedly differs from that of the preceding two configurations. This discrepancy arises from the utilization of the roll-bond evaporator of Type 1, which absorbs heat from the evaporated basin water within the SSTDS cabin to the water heating in the tank.

The maximum calculated water temperatures are 5.23 °C for Type 1, 32.29 °C for Type 2, and 26.67 °C for solar still, respectively. In January, the absence of water preheating resulted in an 83.80% reduction in the basin water temperature compared to instances where preheating was implemented. Figure 7b–d depicts consistent temperature distributions over time for April, July, and October, respectively.

Fig. 6 a The hourly mean ambient temperature with 25th–75th and 10th–90th percentile intervals. **b** The hourly mean solar irradiation with 25th–75th and 10th–90th percentile intervals. **6c** The hourly mean wind speed with 25th–75th and 10th–90th percentile intervals
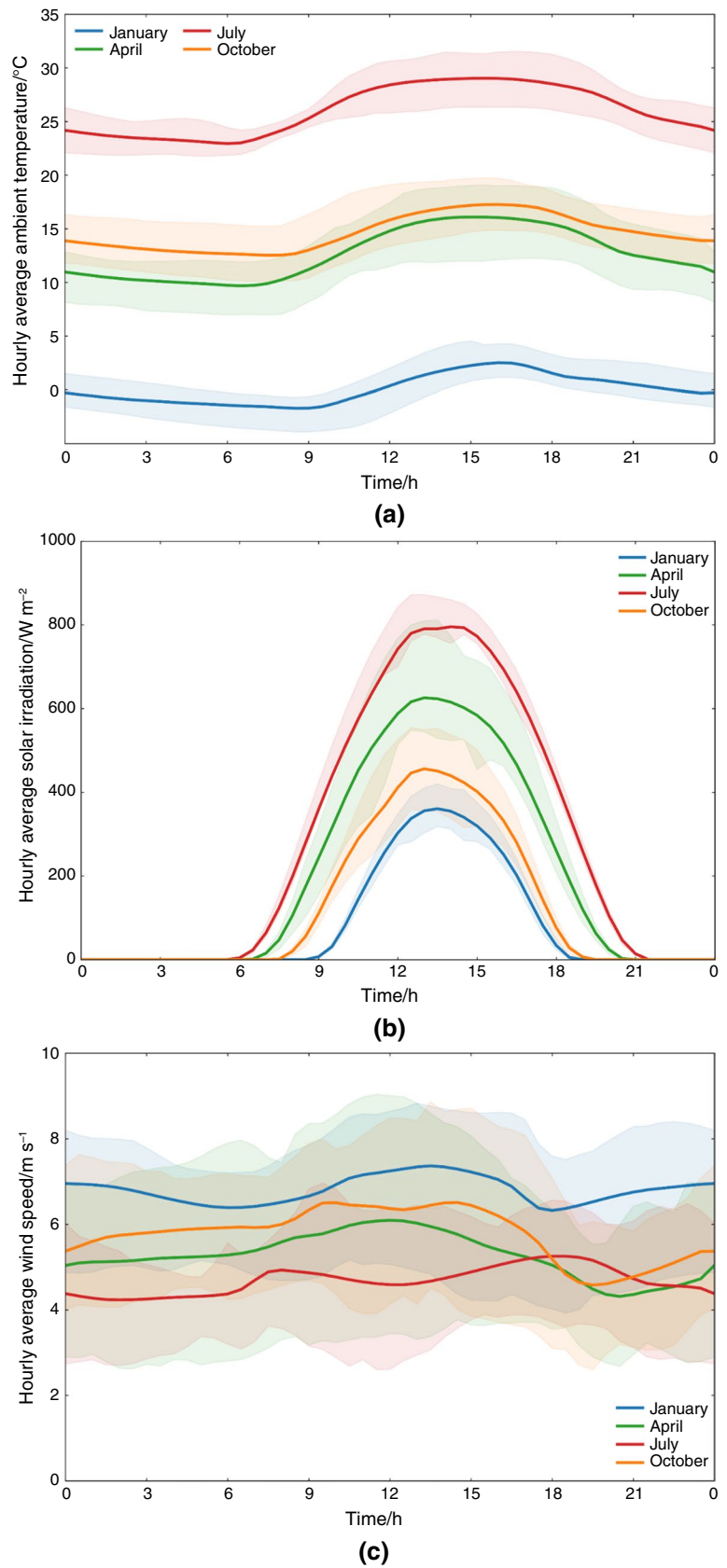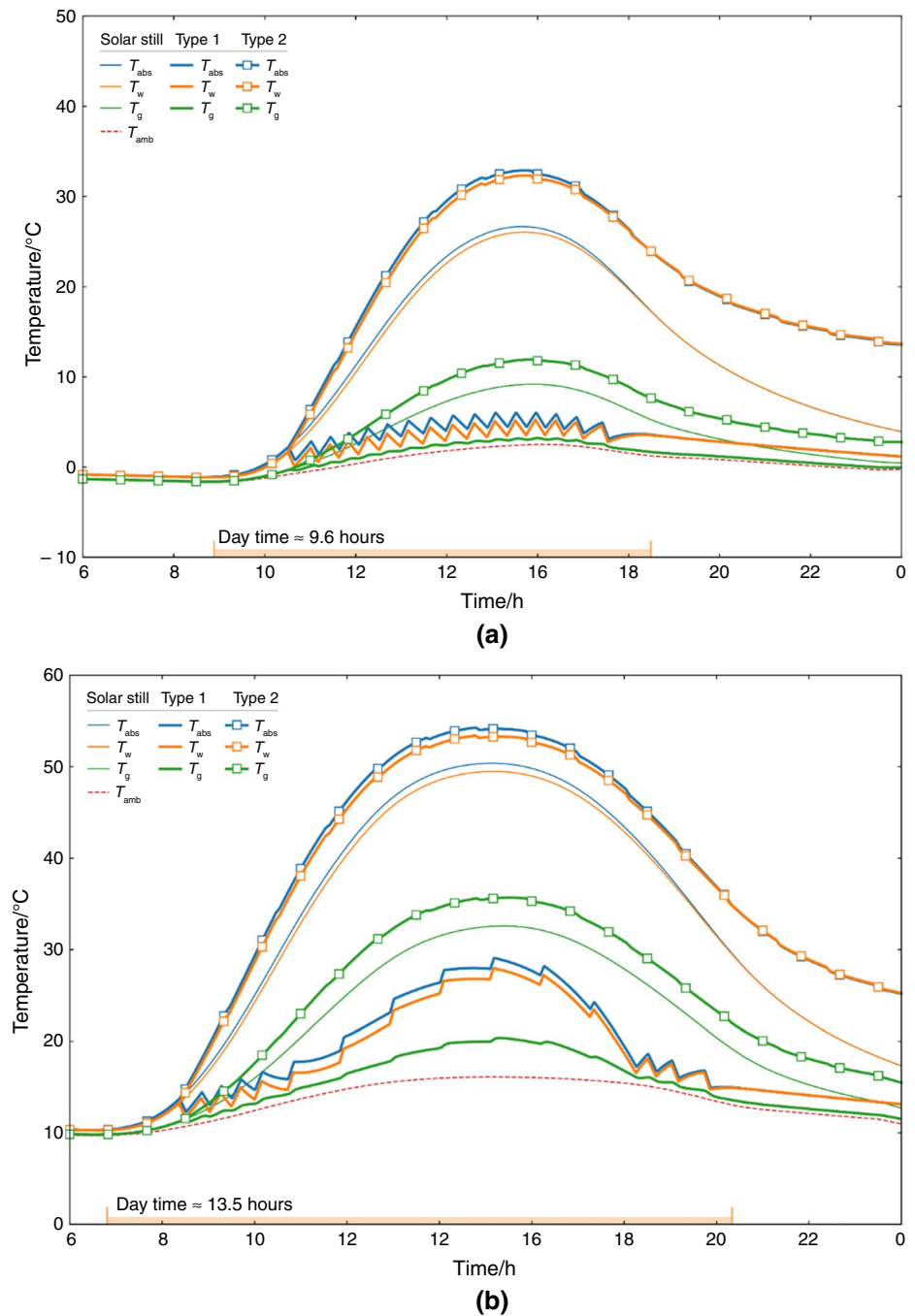

(a)

(b)

(c)

Fig. 7 The temporal temperature fluctuations of various components within the CHP-SSTDS during the month of **a** January, **b** April, **c** July, **d** October


(a)

(b)

As depicted in Fig. 7, across all four seasons, temperatures T_{abs} and T_w exhibit close proximity in value. Conversely, in the Type 1 configuration, these temperatures display fluctuating patterns attributed to the operation of the "Switch" component outlined previously. Across all four scenarios, the absorber temperature consistently surpasses the basin water temperature by approximately 0.84–2.38%.

When comparing the glass temperature across all instances, it consistently exceeds the ambient atmospheric air temperature but remains lower than the basin water temperature. In January, the disparity between the maximum temperatures of water and glass is 65.1% for SS, 38.62% for Type 1, and 63.12% for Type 2. A larger disparity between the temperatures of basin water and glass enhances condensation on the inner surface of the glass, consequently leading to increased productivity. The condensation efficiency escalates when heated vapor encounters a chilled surface. Equivalent metrics for April, July, and October are 34.6%/27.25%/33.16%, 19.72%/19.93%/18.58%, and 35.58%/9.77%/35.26%, respectively.

Fig. 7 (continued)

(c)

(d)
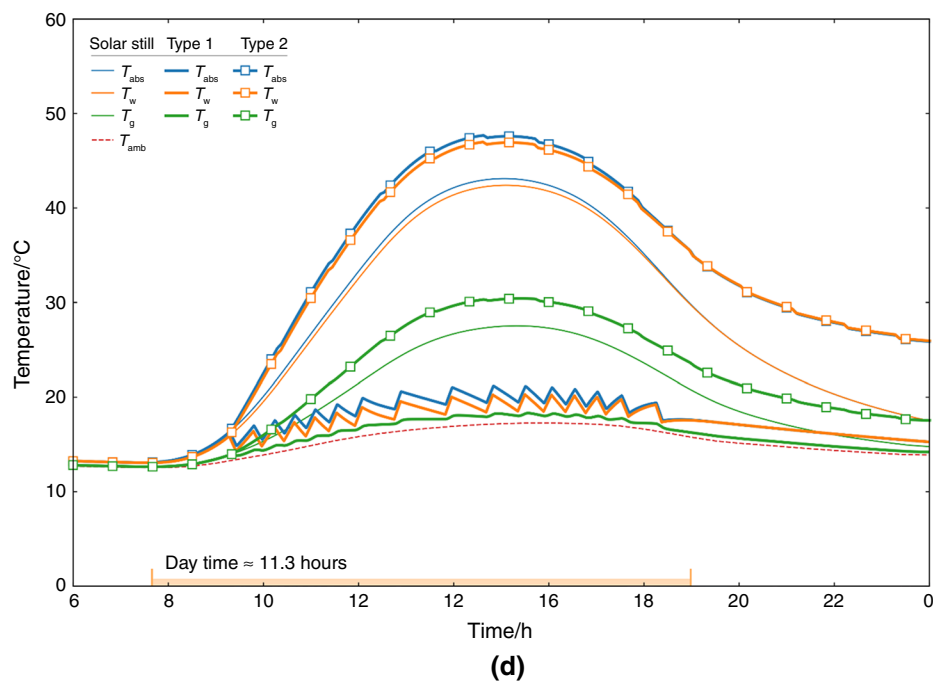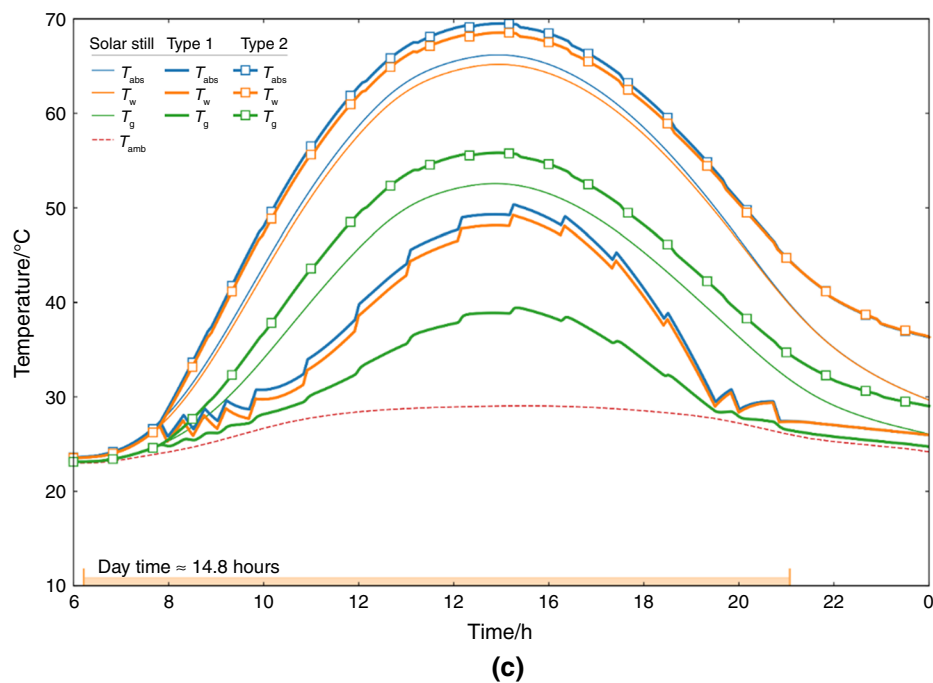
As depicted in Fig. 7a and d, throughout colder months, within Type 1 configuration, the temperatures of the absorber, water, and glass exhibit minimal disparity in their values. Additionally, temperatures T_{abs} and T_w demonstrate a fluctuating pattern of change. The fluctuating pattern observed in the temperature variations of the last two SS components is attributed to the utilization of the "Switch" module, as elaborated earlier. During colder months, reduced solar heat influx into the distiller cabin prompts the roll-bond evaporator to efficiently extract heat, thereby rapidly cooling the water and absorber temperatures to match the glass temperature. In January, the maximum temperatures recorded for the absorber, water, and glass are 6.01 °C, 5.23 °C, and 3.21 °C, respectively. Correspondingly, in October, these temperatures are 21.15 °C, 20.27 °C, and 18.29 °C, respectively. For comparison, during warmer months such as April and July, temperatures T_{abs} and T_w exhibit considerable disparity from T_g. Additionally, T_{abs} and T_w demonstrate a lesser degree of fluctuation, indicating a more stable operation of the heat pump with reduced on/off conditions. In July, the

Table 2 Temperature comparison

Temperature °C	January		April		July		October	
	Min	Max	Min	Max	Min	Max	Min	Max
Conventional solar still								
Glass	− 1.63	9.16	9.78	32.57	23.09	52.53	12.62	27.50
Water	− 1.16	26.04	10.26	49.46	23.53	65.15	13.03	42.38
Absorber	− 1.15	26.66	10.27	50.35	23.55	66.16	13.04	43.09
Heat pump Type 1								
Glass	− 1.63	3.21	9.78	20.34	23.09	39.41	12.62	18.29
Water	− 1.16	5.23	10.26	27.96	23.53	49.22	13.03	20.27
Absorber	− 1.15	6.01	10.27	29.05	23.55	50.31	13.04	21.15
Heat pump Type 2								
Glass	− 1.63	11.91	9.78	35.67	23.09	55.80	12.62	30.40
Water	− 1.16	32.29	10.26	53.37	23.53	68.52	13.03	46.96
Absorber	− 1.15	32.84	10.27	54.24	23.55	69.49	13.04	47.66
Ambient	− 1.72	2.50	9.66	16.09	22.94	29.03	12.52	17.25

maximum temperatures recorded for the T_{abs}, T_w, and T_g are 50.31 °C, 49.23 °C, and 39.41 °C, respectively. Correspondingly, in April, these temperatures are 29.05 °C, 27.96 °C, and 20.34 °C, respectively. Table 2 presents the temperature values of predicted in three configurations at different climatic conditions are given.

Figure 8 illustrates the temporal variations in productivity across all four seasons for the three configurations. For Type 1 and Type 2 configurations, the dynamic productivity surpasses that of a conventional distiller, attributable to the supplementary condensation of water vapor on the surface of the roll-bond evaporator [33, 34]. Nevertheless, the productivity of Type 2 significantly exceeds that of Type 1, attributed to enhanced heat regeneration facilitated by positioning a condenser at the bottom of the SS basin. As illustrated in Fig. 8, the durations of the heat pump's activation and deactivation periods are short and approximately equal for Type 1 during cold months and in the mornings and evenings of warm days (April and July). This occurrence stems from the significant cooling of the SS cabin by the heat pump without additional heating. In contrast, for Type 2 with heat regeneration, the duration of the heat pump's operation exceeds that of its inactivity for all seasons and times of the day. To compare the numerical values, the maximum dynamic productivity for Type 1 during January is 0.0049 [g (m^{-2} 30^{-1} s^{-1})], in April is 0.0056 [g (m^{-2} 30^{-1} s^{-1})], in July is 0.0076 [g (m^{-2} 30^{-1} s^{-1})], and in October is 0.0050 [g (m^{-2} 30^{-1} s^{-1})]. Correspondingly, the analogous metrics for Type 2 are 0.0071 [g (m^{-2} 30^{-1} s^{-1})], 0.011 [g (m^{-2} 30^{-1} s^{-1})], 0.014 [g (m^{-2} 30^{-1} s^{-1})], and 0.009 [g (m^{-2} 30^{-1} s^{-1})], respectively.

As observed in Fig. 8c, the maximum dynamic productivity for conventional solar still and Type 1 are nearly identical. This phenomenon arises from the substantial solar radiation received by the solar still cabin during the summer months.

Despite water vapor condensation occurring on both the inner surface of the glass and the evaporator surface, the productivity of these configurations is nearly indistinguishable during peak solar hours. However, outside of peak sun hours, Type 1 exhibits higher productivity compared to SSTDS. The marginal advantage of incorporating a heat pump in Type 1 configuration implies that a conventional SS can function adequately without an additional evaporator during warmer seasons. The maximum dynamic productivity for conventional SS during January is 0.0013 [g (m^{-2} 30^{-1} s^{-1})], in April is 0.0048 [g (m^{-2} 30^{-1} s^{-1})], in July is 0.0078 [g (m^{-2} 30^{-1} s^{-1})], and in October is 0.0029 [g (m^{-2} 30^{-1} s^{-1})].

If dynamic productivity represents a measure throughout the day, then cumulative productivity serves as an indicator of the total productivity by day's end. Figure 9 illustrates the cumulative daily productivity across the four seasons and the three configurations outlined. As depicted in Fig. 9, the cumulative productivity of conventional solar still is 0.8 [kg (m^{-2} day^{-1})] in January, 3.8 [kg (m^{-2} day^{-1})] in April, 6.9 [kg (m^{-2} day^{-1})] in July, and 2.0 [kg (m^{-2} day^{-1})] in October. For warmer months, these values align with those documented in the open literature and outlined in the Introduction section. As highlighted in the Introduction, the majority of solar still research has been conducted in regions characterized by hot climates. One of the novel aspects of the presented study is the evaluation of the productivity of solar still with and without a heat pump in cold climatic regions exhibiting distinct seasonal variations. As evident from the figure, during the cold month of January, the productivity is notably low, at 0.8 [kg (m^{-2} day^{-1})]. Hence, employing a roll-bond heat pump evaporator, which also facilitates condensate accumulation, is expected to enhance freshwater productivity. However, based on the calculated data

Fig. 8 Temporal variation in instantaneous productivity during **a** January, **b** April, **c** July, **d** October


(a)

(b)
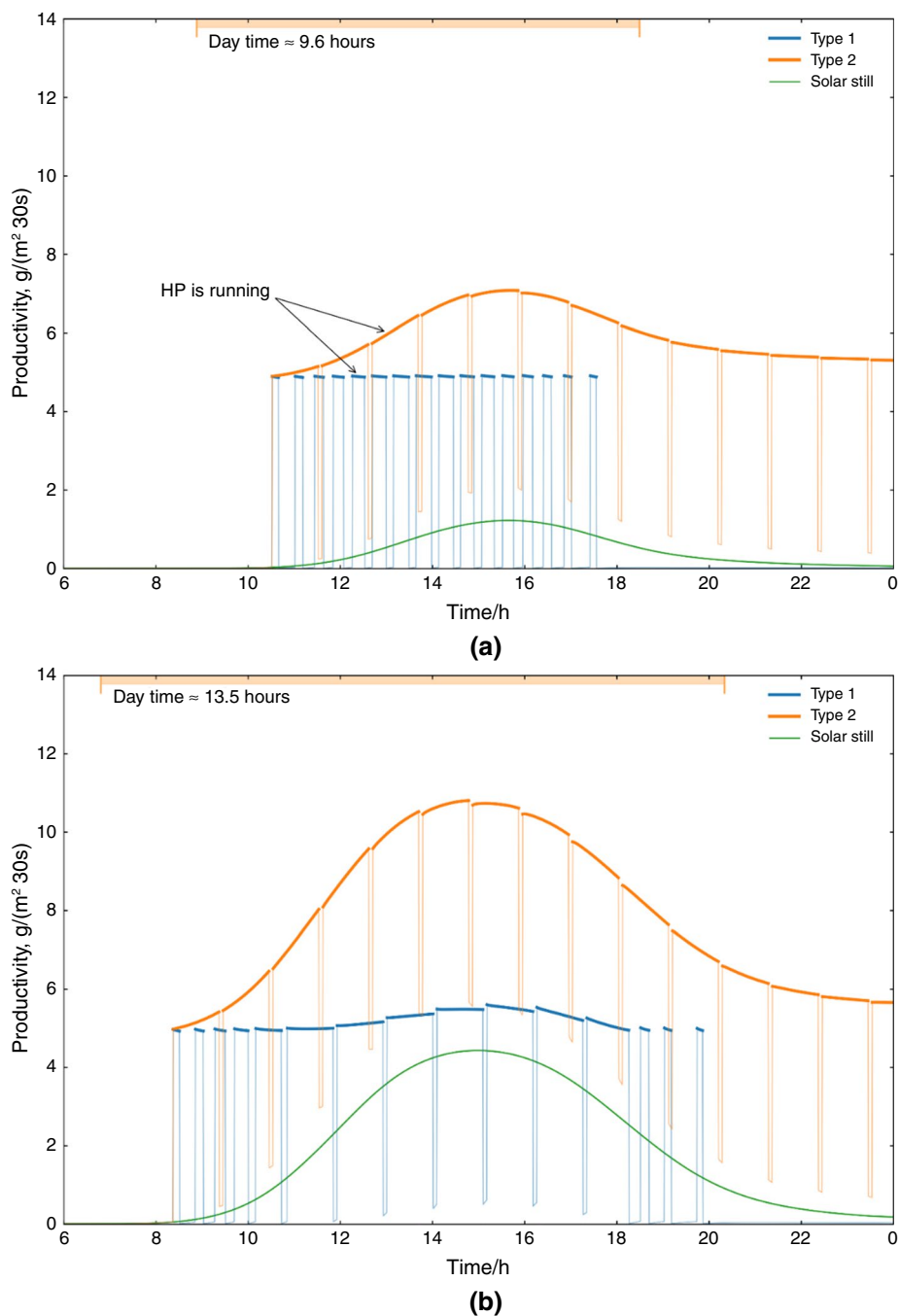
for Type 2, the productivity exhibits a notable increase compared to Type 1. During January, activating the heat pump as per Type 1 resulted in a 63.6% increase in the productivity of conventional solar still, yielding a cumulative productivity of 2.2 [kg (m^{-2} day^{-1})]. Conversely, for Type 2, the increase amounts to 91.1%, resulting in productivity of 9.0 [kg (m^{-2} day^{-1})]. This implies that employing a roll-bond evaporator and achieving complete heat regeneration by reinjecting heat from the condenser to heat the basin water can substantially enhance productivity in cold climates.

Based on the numerical data extracted from Fig. 9b–d, it is evident that Type 2 preheating of basin water markedly augments productivity, even during warmer months. In April, there was a productivity increase of 30.9% for Type 1, resulting in a value of 5.5 [kg (m^{-2} day^{-1})], whereas for Type 2, the increase was 73%, yielding a value of 14.1 [kg (m^{-2} day^{-1})]. In July, the respective figures for Type 1 indicate an 11.5% increase, resulting in 7.8 [kg (m^{-2} day^{-1})], while for Type 2, the increase stands at 61.6%, yielding 18 [kg (m^{-2} day^{-1})]. In October, Type 1 exhibits a 41.2% increase, reaching 3.4 [kg (m^{-2} day^{-1})],

Fig. 8 (continued)
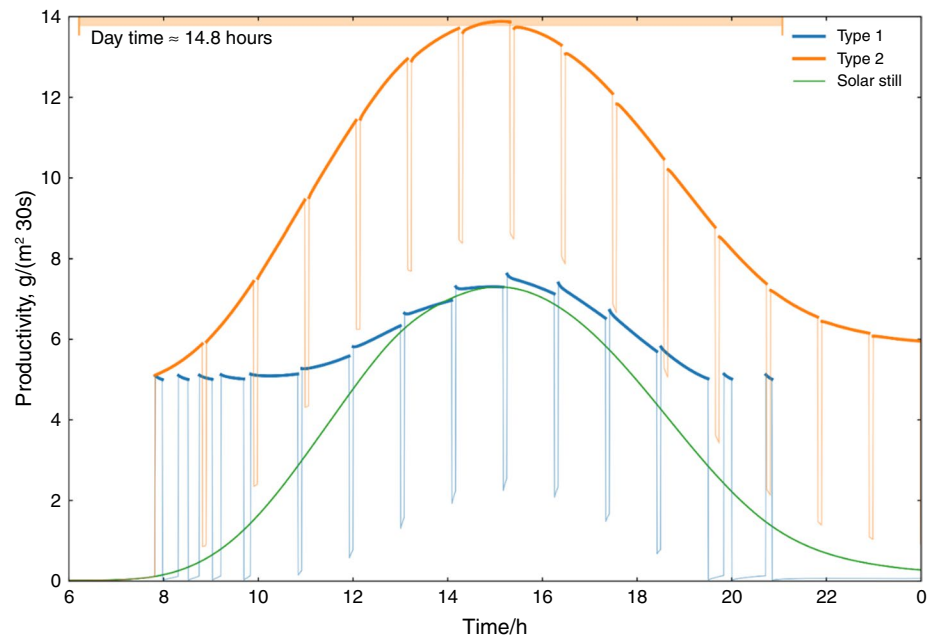
(c)
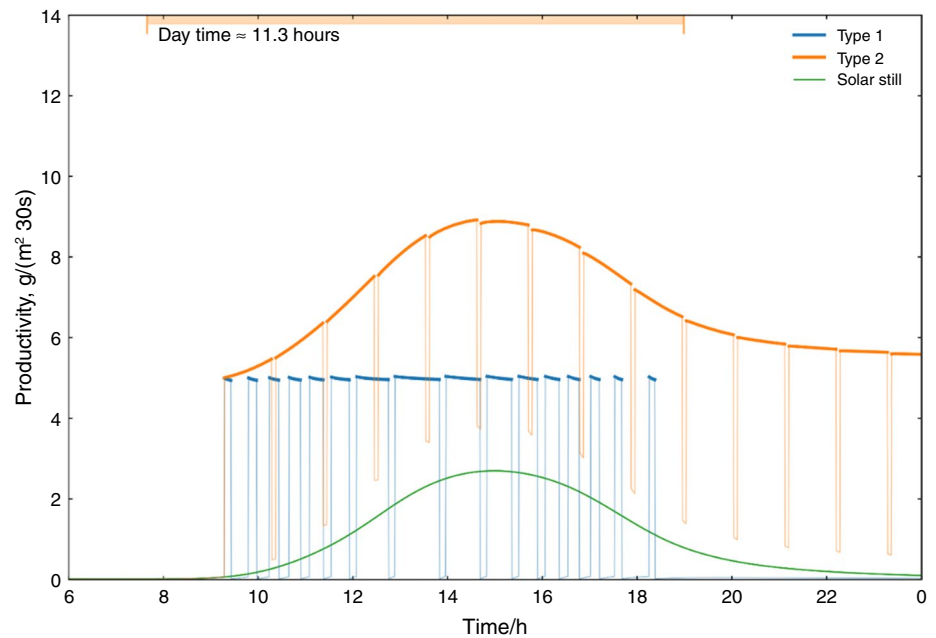
(d)

whereas Type 2 showcases an 82.6% increase, achieving 11.5 [kg (m^{-2} day^{-1})].

Based on the findings, the least enhancement achieved through the utilization of a heat pump compared to a solar still was observed in July for Type 1, amounting to merely 11.5%. Simultaneously, Type 2 attained the peak daily productivity of 18 [kg m^{-2}]. Based on the conducted calculations, it can be inferred that to augment the productivity of the solar distiller, especially in regions characterized by cold climates, the integration of solar still with a heat pump in a Type 2 configuration is imperative.

Subsequently, a parametric investigation was conducted to assess the impact of basin water depth, insulation thickness, and heat pump evaporator capacity on the productivity of the solar desalination device. Figure 10 illustrates the numerical outcomes of the parametric study. Figure 10a depicts the conventional SS normalized daily productivity as a function of basin water depth. In the calculations,

Fig. 9 Cumulative productivity accumulated throughout the day in **a** January, **b** April, **c** July, **d** October


(a)

(b)
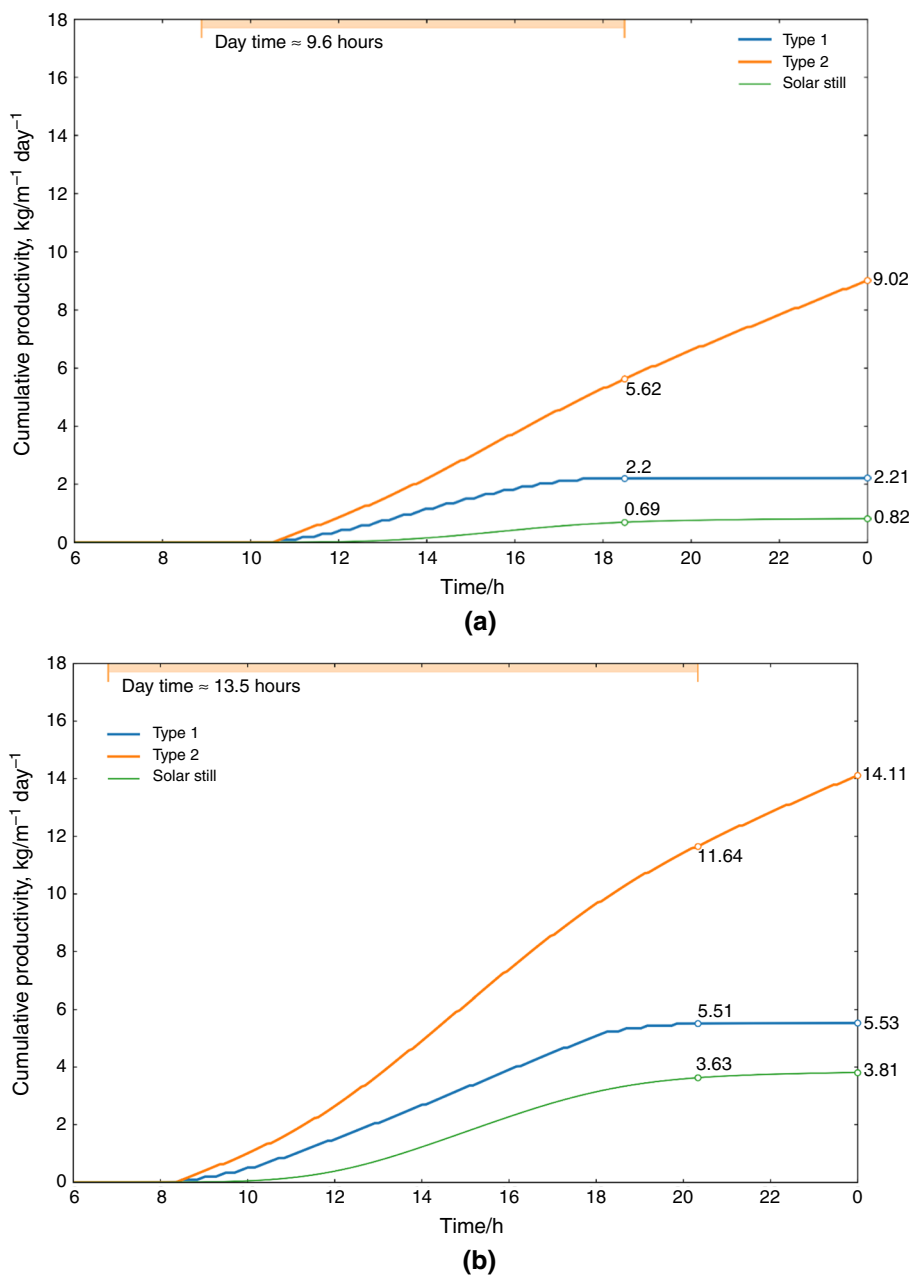
the depth variation ranged from 0.2 to 30 cm. Productivity was normalized relative to the maximum productivity value across all specified water depths. Analysis of the graphs suggests an exponential relationship between these parameters. Productivity peaks at shallower depths due to faster evaporation rates. However, such shallow depths struggle to retain temperature and rapidly transfer heat to surrounding components. Optimal productivity is achieved with water depths less than 10 cm. Comparable findings have been reported by other researchers [1, 40]. In our study, a depth of 2.0 cm was employed in the calculations, while depths of 2.0 cm, 4.0 cm, 6.0 cm, and 10.0 cm were utilized for validation purposes.

As illustrated in Fig. 10a, increasing the basin water depth during warmer seasons exerts a comparatively lesser impact on productivity than during colder seasons. For instance, at a depth of 5.0 cm, normalized daily productivity in January is 47% of the maximum, whereas in July, it reaches 81%. Prior to constructing a solar still, a crucial consideration involves determining the optimal insulation thickness to minimize material usage. This consideration holds particular significance for colder regions, where lower external temperatures result in a notable escalation in heat loss. As indicated in Fig. 10b, insulation thickness exceeding 10.0 cm exhibits minimal influence on productivity. A thickness of 5.0 cm was selected for calculations

Fig. 9 (continued)
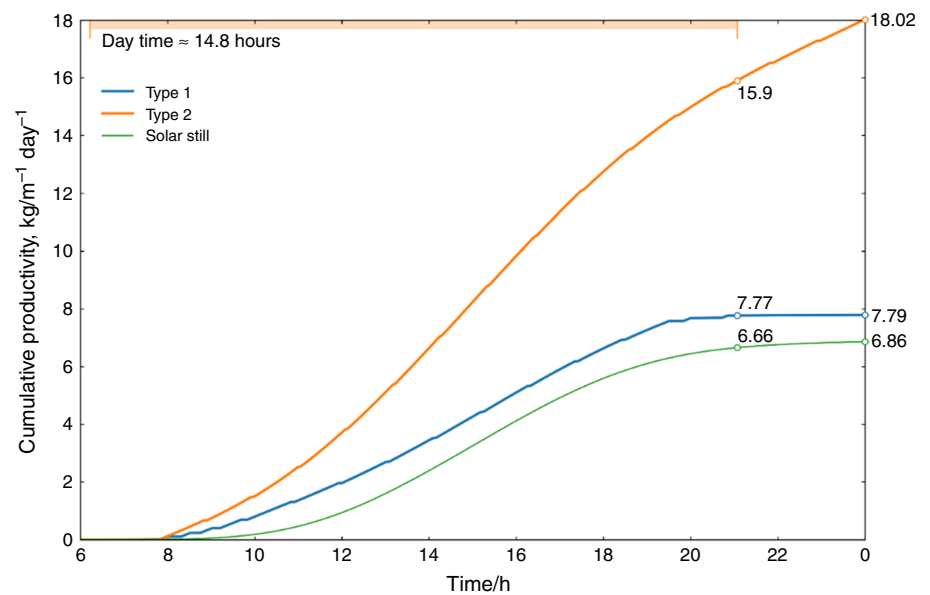
(c)
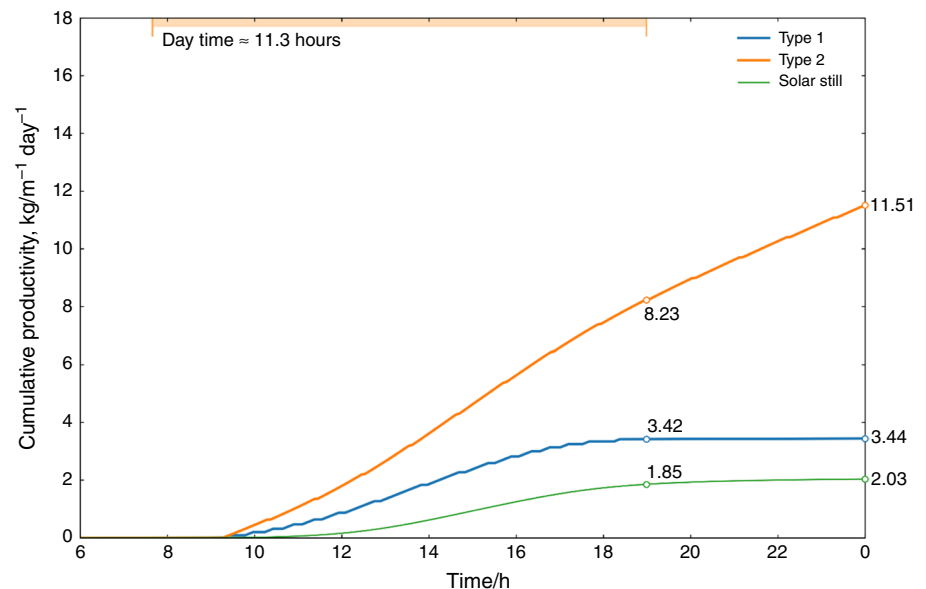
(d)

based on the findings of various experimental studies conducted by other researchers [1, 40]. In this case, productivity is normalized relative to the minimum productivity value across all specified insulation thicknesses. As shown in Fig. 10b, the effect of insulation is significantly greater in cold seasons compared to warm seasons. For example, with an insulation thickness of 2 cm, productivity in January is 8.4 times higher than without insulation, whereas in July, it is 3.52 times higher. At an insulation thickness of 5 cm, similar indicators are 9.8 times higher in January and 3.81 times higher in July. Furthermore, it is evident for all seasons that an increase in thickness beyond 6 cm has minimal effect on productivity.

The foregoing analysis elucidated the outcomes stemming from the implementation of heat pump systems in Type 1 and Type 2 configurations across varying seasons. Based on the accrued data, employing Type 2 configurations with heat regeneration mechanisms emerged as the most efficacious approach for augmenting the productivity of solar still. This conclusion finds support in Fig. 10c, which illustrates the relationship between freshwater productivity and the capacity of the roll-bond evaporator. In the case of Type 2, enhancing the evaporator capacity from 200 to 800 W led to a linear elevation in productivity, surging from 12–13 to over 20 [kg (m^{-2} day^{-1}))]. However, in the case of Type 1, augmenting the evaporator capacity yielded only marginal

Fig. 10 **a** The correlation between solar still productivity and water depth. **b** The correlation between solar still productivity and insulation thickness. **c** The correlation between solar still productivity and evaporator capacity
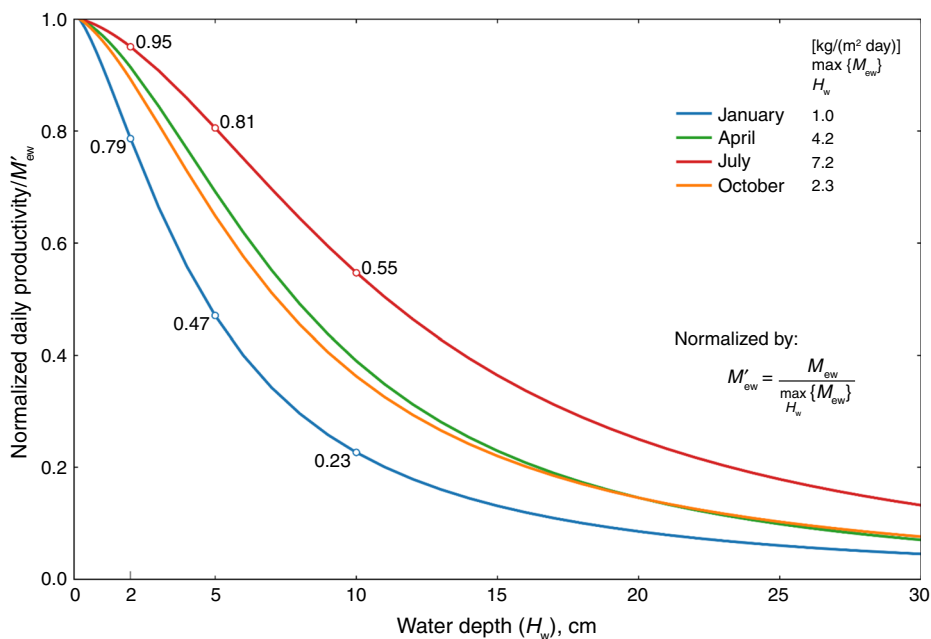

(a)
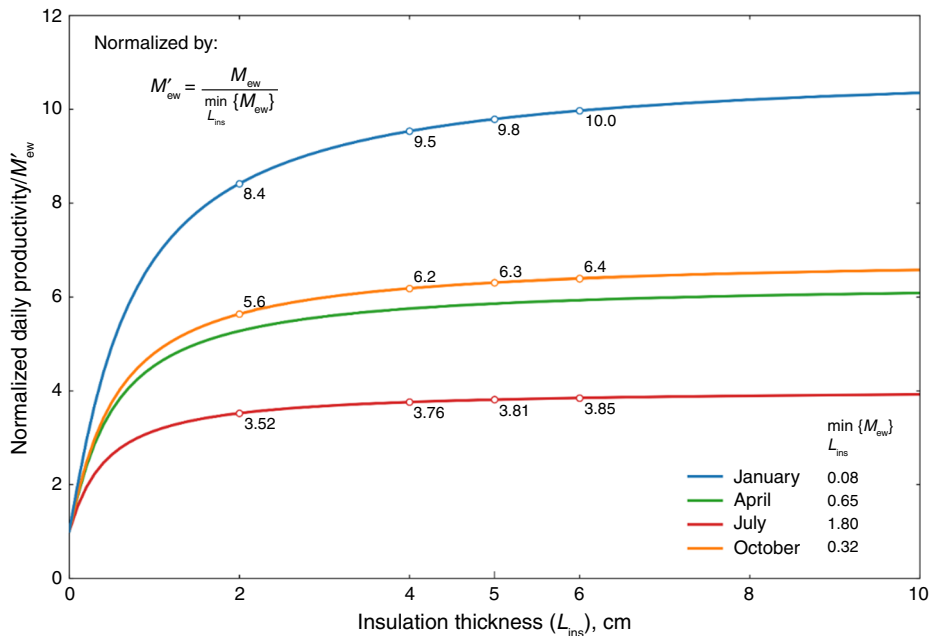
(b)

enhancements in productivity. As depicted in Fig. 10c, in both configurations, activating the heat pump evaporator during cold seasons offers a greater advantage over conventional solar still compared to warm seasons. Simultaneously, Type 1 exhibits a limitation; beyond an evaporator capacity of 400 W, the increase in productivity becomes insignificant. At a capacity of 400 W in January, the enhancement is 2.71

times compared to a conventional still, whereas in July, this enhancement reaches 1.13 times. For Type 2, comparable enhancements at 400 W are 11.0 times in January and 2.6 times in July, respectively. With an increasing evaporator capacity, productivity for Type 2 exhibits further linear increases for all seasons.

Fig. 10 (continued)

(c)
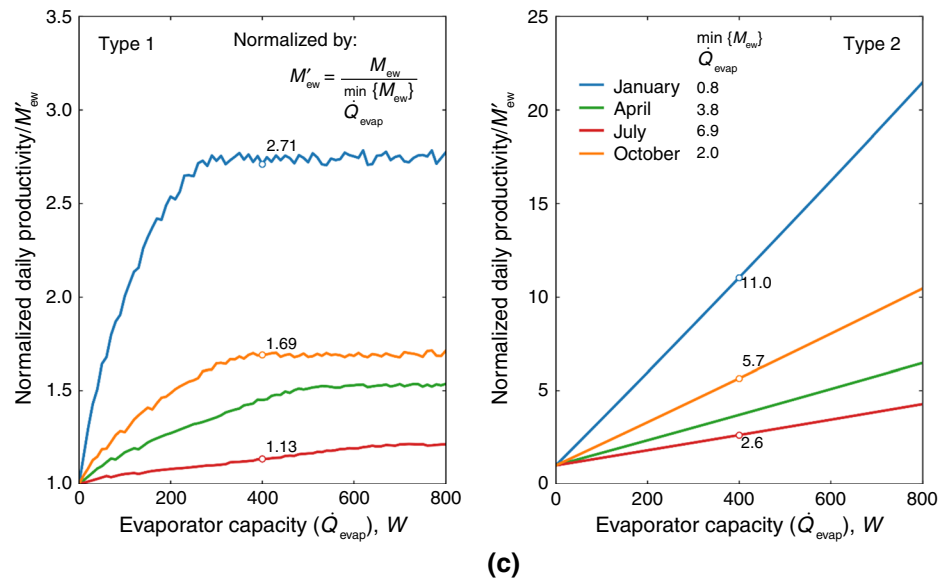
Conclusions

The numerical performance simulation of a solar still, heat pump-assisted solar still, and heat pump-assisted regenerative solar still was performed under the climatic conditions of Aktau City in Kazakhstan. The mathematical model was developed based on the first law of thermodynamics using energy balance equations. Based on the numerical study, the following major conclusions were made:

i. The numerical simulation model predicts the performance of a solar still within $\pm 20\%$ deviations.
ii. The integration of the compression heat pump with the solar still (with regeneration) has 91.1% improved freshwater production than conventional solar still.
iii. The integration of the compression heat pump with the solar still (without heat regeneration) has 63.6% improved freshwater production than conventional solar still.
iv. During the summer season, the compression heat pump-assisted regenerative solar still (with regeneration) has 61.6% improved freshwater production.
v. Maximum freshwater production was noticed with water depths between 0.5 and 2 cm.
vi. The thickness of glass-wool insulation was optimized in the range between 5 and 7 cm.
vii. An increase in evaporator capacity has increased freshwater production.

The results confirmed that the proposed numerical simulation tool is suitable for investigating the feasibility of compression heat pump-assisted solar still in various water scarcity cities of Kazakhstan. Further, the prototype development and economic and environmental impacts of the proposed system are to be assessed for commercialization. Such, research investigations are in progress at the authors research laboratory with the support of the Ministry of Science and Higher Education, Republic of Kazakhstan.

Appendix A

$$\varepsilon_{\mathrm{eff}} = \frac{1}{\left[\frac{1}{\varepsilon_{\mathrm{w}}} + \frac{1}{\varepsilon_{\mathrm{g}}} - 1\right]}$$

$$T_{\mathrm{avg}} = \frac{T_{\mathrm{w}} + T_{\mathrm{abs}}}{2}$$

$$\mathrm{Ra}_{\mathrm{w}} = Gr_{\mathrm{w}} \cdot Pr_{\mathrm{w}}$$

$$L'_{\mathrm{w}} = \frac{A_{\mathrm{w}}}{2(L_{\mathrm{w}} + W_{\mathrm{w}})}$$

$$Gr_{\mathrm{w}} = \frac{g\beta\rho^2 L'_{\mathrm{w}}\left|T_{\mathrm{pl}} - T_{\mathrm{w}}\right|}{\mu^2}$$

$$Pr_{\mathrm{w}} = \frac{\mu C_{\mathrm{w}}}{k_{\mathrm{w}}}$$

Seawater properties

Density [45]:

$$\rho_w\{T_{avg}\} = 1000 \cdot (0.5a + Ab + c(2A^2 - 1) + d(4A^3 - 3A))$$

where:

$$\begin{cases} A = \frac{2T_{avg}-200}{160} \\ B = \frac{2S-150}{150} \\ a = 2.016110 + 0.115313 \cdot B + 0.000326(2B^2 - 1) \\ b = -0.0541 + 0.001571 \cdot B - 0.000432(2B^2 - 1) \\ c = -0.006124 + 0.001740 \cdot B - 0.9 \cdot 10^{-5}(2B^2 - 1) \\ d = 0.000346 + 0.87 \cdot 10^{-4}B - 0.53 \cdot 10^{-4}(2B^2 - 1) \end{cases}$$

Thermal conductivity [45]:

$$k_w = (k_c + a)e^{\left(2.3 - \frac{b}{(T_{avg}+273.15)}\right) \cdot \left(1 - \frac{T_{avg}+273.15}{T_c+c}\right)}$$

where:

$$\begin{cases} k_c = 0.24 \\ T_c = 647.3[K] \\ a = 0.0002 \cdot S \\ b = 343.5 + 0.375 \cdot S \\ c = 0.03 \cdot S \end{cases}$$

Water dynamic viscosity [45]:

$$\mu = \mu_{pw}(1 + a \cdot S + b \cdot S^2)$$

where:

$$\begin{cases} \mu_{pw} = 4.2544 \cdot 10^{-5} + \left[0.157(T_{avg} + 64.993)^2 - 91.296\right]^{-1} \\ a = 0.001474 + 1.5 \cdot 10^{-5} \cdot T_{avg} - 0.003927 \cdot 10^{-5} \cdot T_{avg}^2 \\ b = 1.0734 \cdot 10^{-5} - 8.5 \cdot 10^{-8} \cdot T_{avg} + 0.00223 \cdot 10^{-7} \cdot T_{avg}^2 \end{cases}$$

Latent heat of vaporization [34, 46]:

$$h_{fg} = \left(1 - \frac{S}{1000}\right)\big(2.501 \cdot 10^6 - 2.369 \cdot 10^3 T_{avg} \\ + 2.678 \cdot 10^{-1}T_{avg}^2 - 8.103 \cdot 10^{-3}T_{avg}^3 - 2.079 \cdot 10^{-5}T_{avg}^4\big)$$

Specific heat capacity of saline water [47]:

$$C_w = 1000 \cdot (a + b(T_{avg} + 273.15) \\ + c(T_{avg} + 273.15)^2 + d(T_{avg} + 273.15)^3)$$

where:

$$\begin{cases} a = 5.328 - 9.76 \cdot 10^{-2} \cdot S + 4.04 \cdot 10^{-4} \cdot S^2 \\ b = -6.913 \cdot 10^{-3} + 7.351 \cdot 10^{-4} \cdot S - 3.15 \cdot 10^{-6} \cdot S^2 \\ c = 9.6 \cdot 10^{-6} - 1.927 \cdot 10^{-6} \cdot S + 8.23 \cdot 10^{-9} \cdot S^2 \\ d = 2.5 \cdot 10^{-9} + 1.666 \cdot 10^{-9} \cdot S - 7.125 \cdot 10^{-12} \cdot S^2 \end{cases}$$

Thermal expansion coefficient:

$$\beta = \frac{\left(\rho_w\{T_{avg} - 0.1\} - \rho_w\{T_{avg}\}\right)}{0.1} \cdot \rho_w\{T_{avg}\}$$

Pressure [47]:

$$P_i = \frac{611.21 \cdot e^{\left[\left(18.678 - \frac{T_i}{234.5}\right)\left(\frac{T_i}{T_i+257.14}\right)\right]}}{1 + 0.57257 \cdot \frac{S}{1000-S}}$$

or [48]

$$P_i = e^{\left[25.317 - \frac{5144}{T_i+273.15}\right]}$$

References

1. Mohanraj M, Karthick L, Dhivagar R. Performance and economic analysis of a heat pump water heater assisted regenerative solar still using latent heat storage. Appl Therm Eng. 2021;196: 117263.
2. Mohanraj M, Belyayev Ye, Jayaraj S, Kaltayev A. Research and developments on solar assisted compression heat pump systems–A comprehensive review (Part-B: applications). Renew Sustain Energy Rev. 2018;83:124–55.
3. Arjunan TV, Aybar HS, Nedunchezhian N. Status of solar desalination in India. Renew Sustain Energy Rev. 2009;13:2408–24.
4. Saxena A, Cuce E, Kabeel AE, Abdelgaied M, Goel V. A thermodynamic review on solar stills. Sol Energy. 2022;237:377–413.

5. Tei EA, Hameed RMS, Illyas M, Athikesavan MM. Experimental investigation of inclined solar still with and without sand as energy storage materials. J Energy Storage. 2024;77: 109809.

6. Sambare RK, Joshi S, Kanojiya NC. Improving the freshwater production from tubular solar still using sensible heat storage materials. Therm Sci Eng Prog. 2023;38: 101676.

7. Arunkumar T, Wang J, Rufuss DDW, Denkenberger D, Kabeel AE. Sensible desalting: investigation of sensible thermal storage materials in solar stills. J Energy Storage. 2020;32: 101824.

8. Sakthivel M, Shanmugasundram S. Effect of energy storage medium (black granite gravel) on the performance of a solar still. Int J Energy Res. 2008;32:68–82.

9. Katekar VP, Deshmukh SS. A review of the use of phase change materials on performance of solar stills. J Energy Storage. 2020;30: 101398.

10. Kabeel AE, El-Samadonya YAF, El-Maghlany WM. Comparative study on the solar still performance utilizing different PCM. Desalination. 2018;432:89–96.

11. Sakthivel M, Shanmugasundaram S, Alwarsamy T. An experimental study on a regenerative solar still with energy storage medium—jute cloth. Desalination. 2010;264:24–31.

12. Modi KV, Patel SK, Patel AM. Impact of modification in the geometry of absorber plate on the productivity of solar still—a review. Sol Energy. 2023;264: 112009.

13. Kateshia J, Lakhera VJ. Analysis of solar still integrated with phase change material and pin fins as absorbing material. J Energy Storage. 2020;35: 102292.

14. Peng G, Sharshir SW, Wang Y, An M, Ma D, Zang J, Kabeel AE, Yang N. Potential and challenges of improving solar still by micro/nano-particles and porous materials—a review. J Clean Prod. 2021;311: 127432.

15. Dhivagar R, Mohanraj M. Performance improvements of single slope solar still using graphite plate fins and magnets. Environ Sci Pollut Res. 2021;28:20499–516.

16. Abdullah AS. Improving the performance of stepped solar still. Desalination. 2013;319:60–5.

17. Kabeel AE, Mohamed A, Mahgoub M. The performance of a modified solar still using hot air injection and PCM. Desalination. 2016;379:102–7.

18. Rajaseenivasan T, Raja PN, Srithar K. An experimental investigation on a solar still with an integrated flat plate collector. Desalination. 2014;347:131–47.

19. Sampathkumar K, Senthilkumar P. Utilization of solar water heater in a single basin solar still—an experimental study. Desalination. 2012;297:8–19.

20. Omara ZM, Eltawil MA, ElNashar EA. A new hybrid desalination system using wicks/solar still and evacuated solar water heater. Desalination. 2013;325:56–64.

21. Bait O. Exergy, environ-economic and economic analyses of a tubular solar water heater assisted solar still. J Clean Prod. 2019;212:630–46.

22. Yildirim C, Solmus I. A parametric study on a humidification-dehumidification (HDH) desalination unit powered by solar air and water heaters. Energy Convers Manage. 2014;86:568–75.

23. Yuan G, Wang Z, Li H, Li X. Experimental study of a solar desalination system based on humidification-dehumidification process. Desalination. 2011;277:92–8.

24. Saidi S, Radhia RB, Ben S, Nafiri N, Benhamou B, Jaballah SB. Numerical study and experimental validation of a solar powered humidification-dehumidification desalination system with integrated air and water collectors in the humidifier. Renew Energy. 2023;206:466–80.

25. Abad KSH, Ghiasi M, Mamouri MJS, Shafii. A novel integrated solar desalination system with a pulsating heat pipe. Desalination. 2013;311:206–10.

26. Behnam P, Shafii MB. Examination of a solar desalination system equipped with an air bubble column humidifier, evacuated tube collectors and thermosyphon heat pipes. Desalination. 2016;397:30–7.

27. Rajan S, Raja K, Marimuthu P. Multi basin desalination using biomass heat source and analytical validation using RSMA. Energy Convers Manage. 2014;87:359–66.

28. Dhivagar R, Mohanraj M, Belyayev Y. Performance analysis of crushed gravel sand heat storage and biomass evaporator assisted single slope solar still. Environ Sci Pollut Res. 2021;28:65610–20.

29. Mohanraj M, Belyayev Ye, Jayaraj S, Kaltayev A. Research and developments on solar assisted compression heat pump systems–A comprehensive review (Part A: modeling and modifications). Renew Sustain Energy Rev. 2018;83:90–123.

30. Hawlader MNA, Dey PK, Diab S, Chung CY. Solar assisted heat pump desalination system. Desalination. 2004;168:49–54.

31. Hidouri K, Slama RB, Gabsi S. Hybrid solar still by heat pump compression. Desalination. 2010;250:444–9.

32. Halima HB, Frikha N, Slama RB. Numerical investigation of a simple solar still coupled to a compression heat pump. Desalination. 2014;337:60–6.

33. Belyayev Ye, Mohanraj M, Jayaraj S, Kaltayev A. Thermal performance simulation of a heat pump assisted solar desalination system for Kazakhstan climatic conditions. Heat Transf Eng. 2019;40:1060–72.

34. Shakir Ye, Saparova B, Belyayev Ye, Kaltayev A, Mohanraj M, Jayaraj S. Numerical simulation of a heat pump assisted regenerative solar still with PCM heat storage for cold climates of Kazakhstan. Therm Sci. 2017;21:411–8.

35. Hidouri K, Mohanraj M. Thermodynamic analysis of a heat pump assisted solar still. Desalin Water Treat. 2019;154:101–10.

36. Sivakumar S, Siva K, Mohanraj M. Energy performance and economic assessments of a solar air collector and compression heat pump integrated solar humidifier desalination systems. J Process Mech Eng. 2023;237:2045–59.

37. Sharshir SW, Tareemi AA, Joseph A, Awad E, Yuan Z, Kandeal AW. Parametric study and thermal performance assessment of a new solar desalination unit coupled with heat pump. Sol Energy. 2023;264: 112033.

38. Sharshir SW, Joseph A, Elsayad MM, Kandeal AW. A new heat pump-operated solar desalination unit integrated with an air recirculating room. Appl Therm Eng. 2024;236: 121487.

39. TRNSYS 18.0, Thermal Energy System Specialists, 2018.

40. Agrawal A, Rana RS, Srivastava PK. Heat transfer coefficients and productivity of a single slope single basin solar still in Indian climatic condition: experimental and theoretical comparison. Resour-Eff Technol. 2017;3:466–82.

41. Dunkle RV Solar water distillation: the roof type still and multiple effect diffusion still international developments in heat transfer. In: ASME, Proceedings of International Heat Transfer, University of Colorado (vol) 5 pp 895 902 1961

42. Shukla SK, Sorayan VPS. Thermal modeling of solar stills an experimental validation. Renew Energy. 2005;30:683–99.

43. Bergman T.L., Lavine A.S., Fundamentals of Heat and Mass Transfer. Wiley, 2017.

44. The data was obtained from the National Aeronautics and Space Administration (NASA) Langley Research Center (LaRC) Prediction of Worldwide Energy Resource (POWER) Project funded through the NASA Earth Science/Applied Science

Program. The data was obtained from the POWER Project's Hourly 2.0.0 version on 2024/05/02.

45. Belessiotis V, Kalogirou S, Delyannis E. Thermal solar desalination. Methods and systems. Academic Press; 2016.
46. Shahrim NA, Abounahia NM, Ahmed El-Sayed AM, Saleem H, Zaidi SJ. An overview on the progress in produced water desalination by membrane-based technology. J Water Process Eng. 2023;51: 103479.
47. Sharqawy MH, Lienhard JHV, Zubair SM. Thermophysical properties of seawater: a review of existing correlations and data. Desalin Water Treat. 2010;16:354–80.
48. Gaur MK, Tiwari GN. Optimization of number of collectors for integrated PV/T hybrid active solar still. Appl Energy. 2010;87:1763–72.